



Joint Activity Scenarios and Modelling

EPFL

PV GENERATION HOSTING CAPACITY OF MEDIUM VOLTAGE DISTRIBUTION GRIDS OF SWITZERLAND

Rahul Kumar Gupta

Fabrizio Sossan

Mario Paolone

Distributed Electrical Systems Laboratory
Ecole Polytechnique Fédérale de Lausanne, Switzerland

December 8, 2020

Supported by:



Schweizerische Eidgenossenschaft
Confédération suisse
Confederazione Svizzera
Confederaziun svizra

Swiss Confederation

Innosuisse – Swiss Innovation Agency

Contents

Contents	ii
1 Estimation of country-wide models of MV distribution networks	2
1.1 Identification of EHV areas	2
1.2 Identification of the locations of the HV/MV primary substations	3
1.2.1 Identification of the HV/MV primary substations	4
1.3 Identification of the HV areas and MV/LV secondary substations	5
1.4 Routing of medium voltage networks	6
1.4.1 Routing algorithm	6
1.4.2 Re-routing unsuccessful networks	9
2 PV hosting capacity and energy storage requirements	13
2.1 Input data	13
2.1.1 Capacity factor of PV production	13
2.1.2 Land-use constraints for PV generation	13
2.1.3 Time series of the PV generation and demand	14
2.2 The PV hosting capacity problem	15
2.3 Increasing PV hosting capacity with BESSs	17
2.3.1 Results	19
2.4 Optimal allocation of PV and BESSs	20
3 Results and Discussion	22
3.1 Case study	22
3.2 Deployment of PV plants	22
3.3 Deployment of PV plants and BESSs for Case 0 and Case 1	24
3.4 Cost comparison	25
4 Conclusions	27

Executive summary

Whilst photovoltaic (PV) energy has a great generation potential, small- and commercial-scale PV plants are normally connected to distribution grids, which are not designed to host significant generation. Modeling the existing distribution infrastructure's technical constraints is critical to ensure the feasibility and economic viability of future energy scenarios. This report presents the work of estimating the PV hosting capacity for Switzerland accounting for the distribution grids' operational constraints.

Estimating the PV generation hosting capacity of existing distribution grids requires the information on network topologies and line parameters of the distribution systems for Switzerland. As these data are not publicly available, we first estimate the MV distribution networks based on spatially distributed information of the electrical demand leveraging information freely available from the Swiss Federal Office of Topography, land-use constraints, location of the extra-high-voltage nodes, and distributed solar irradiance potential. We then estimate the PV generation hosting capacity for entire Switzerland with a state-of-the-art and computationally tractable method based on a linearized optimal power flow (OPF). We model the PV plants as uncontrollable injections operated at maximum power point (MPP). To increase the PV hosting capacity, we compute the optimal size and sites of the battery energy storage systems. The grid reinforcements and curtailments of PV generation is not accounted in this study. We ultimately investigate the economically optimal deployment of PV power plants across Switzerland, including the placement and sizing of battery energy storage systems to increase the generation hosting capacity of those distribution grids with significant solar radiation levels.

Thanks to the developed grid model, it has been possible to estimate a value of 14 GW as the total PV hosting capacity without the need of battery energy storage. Bauer and Hirschberg (2017) estimated a yearly PV production potential from roof-top PV generation of 25 TWh that corresponds to a total installed capacity in the range of 22 – 27 GW. According to our analysis, increasing the PV hosting capacity to 27 GW for achieving this goal requires installing 65 GWh of distributed energy storage with a total power rating of 12 GW (without upgrading the distribution grids). It was found that mitigating grid congestions under the best irradiance conditions (uniform clear-sky) is an energy-intensive application with required battery reservoir size almost 5-times the converter ratings. These battery storage can be coupled well with power-intensive applications in a multiple-grid-service context, such as providing synthetic inertia or primary frequency control.

formed by secondary and tertiary substations to the final level at which electricity is consumed. As opposed to secondary and tertiary substations, the locations of the primary substations are available in public databases (e.g. ENTSOE (2019)). We use them as the first step to infer the rest of the network. In total, we consider 148 georeferenced EHV substations. The locations of the EHV nodes are from the dataset (Wiegmans, 2016), that is derived from ENTSOE information. It was verified by visual inspection from aerial images that not all the locations from Wiegmans (2016) correspond to the real ones, as also acknowledged on the ENTSOE website¹. The inaccurate locations were corrected, when possible, by considering the locations reported in the collaborative dataset², which were found accurate after being verified one by one on aerial images. The locations of the EHV nodes are shown in Fig. 1.2a.

Starting from the locations of the EHV substations, we apply Voronoi diagrams to approximate the region that each EHV node serves. Given an image and a collection of coordinates within that image, a Voronoi diagram (one per set of coordinates) is the closest locus of points to those coordinates. We use Voronoi diagrams because we reasonably assume that the electrical demand in a certain area is served by the closest substation. This modeling choice is also proposed in Amme et al. (2018), Wang et al. (2014), Yan et al. (2019), Chen et al. (2017). The result of the Voronoi partitioning is shown in Fig. 1.2b.

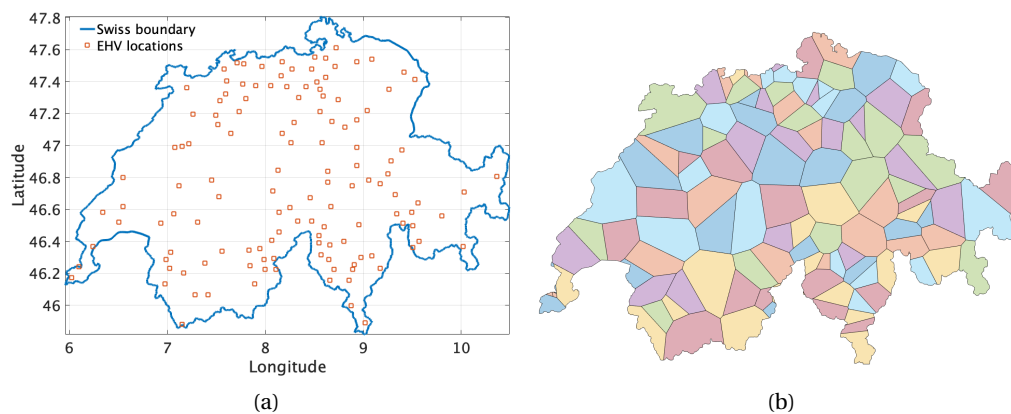


Figure 1.2: Identification of EHV areas: (a) locations of the considered 148 EHV substations in Switzerland and (b) approximated regions served by each substation after Voronoi partitioning.

1.2 Identification of the locations of the HV/MV primary substations

Distribution of the electrical demand

Power distribution systems were designed to deliver electricity to end customers. Therefore, we expect their topology and power ratings to reflect the geographical distribution of the demand for electricity. We leverage this notion and we start from the distribution of the electricity demand over the country to infer the topology of distribution systems. First, we estimate the distribution of the electricity demand as described next.

¹<https://www.entsoe.eu/data/map/>

²https://en.wikipedia.org/wiki/List_of_EHV-substations_in_Switzerland

Table 1.1: Composition of electricity demand in different sectors for Switzerland for 2014 (Eymann et al., 2014).

Sector	Electricity demand (GWh)
Residential	18'333
Commercial	17'531
Industrial	19'028

The work in Eymann et al. (2014) reports the statistics of the sectorial (industrial, commercial and residential) electricity consumption for each canton in Switzerland. This information gives already a comprehensive overview of the country-wide distribution of the electricity demand. However, since power distribution systems extend far deep into local regions, higher spatially resolved data are needed to estimate their topology. The Swiss Federal Office for Topography³ has mapped the heat demand for space heating and cooling for industrial, commercial, and residential buildings with a resolution of 100x100 meters. Since the heat demand follows the building distribution and that buildings are also large consumer of electricity (due to various electrical equipment, besides the obvious case of electric space heating (Wojdyga, 2008, Avdakovic et al., 2013), that reinforces the correlation among the two), we assume that the electricity and heat demands follow the same spatial distribution. With this assumption, we model the electricity demand map by rescaling heat demand map by appropriate coefficients such that its sum over space amounts to the total electricity demand for each sector reported in Table 1.1. The estimated country-wide electricity demand map is shown in Fig. 1.3a. Fig. 1.3b is an illustrative example of the electrical demand distribution within a single Voronoi cell.

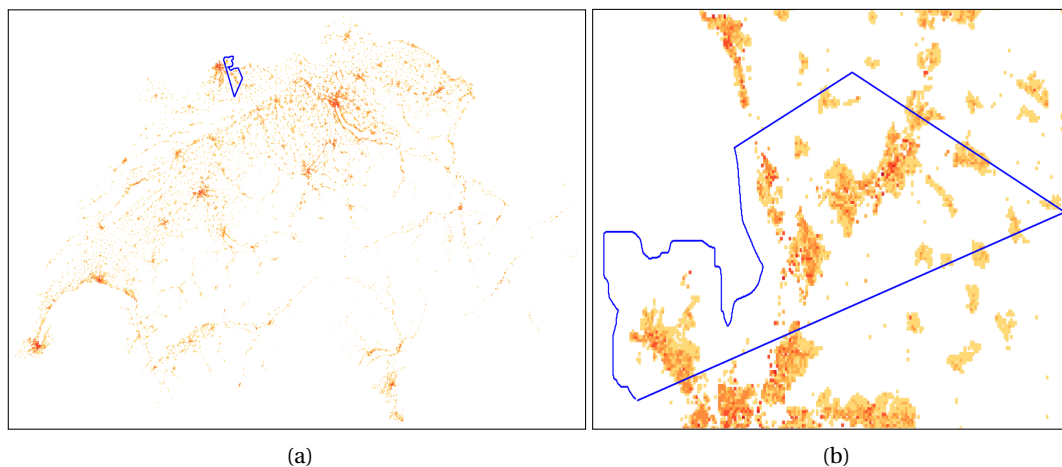


Figure 1.3: Estimated electricity demand map of: (a) Switzerland and (b) a single EHV area. The blue polygon refers to an EHV area obtained using Voronoi partition.

1.2.1 Identification of the HV/MV primary substations

The location of the HV/MV secondary substation is determined by analyzing the electrical demand map within each EHV area according to the following procedure.

³<http://map.geo.admin.ch/>

1. Identify clusters with contiguous demand. To do so, we first derive a binary image from the electrical demand map, where Boolean true pixels denote non-zero electrical demand, and vice-versa. Then, to identify clusters with contiguous demand, we apply binary image segmentation, that partitions the input binary map into clusters containing pixels of the same kind (true or false) only. For the binary image segmentation, we use the `bwboundaries` Matlab function (Gonzalez et al., 2004). The result of this process for the example EHV area of Fig. 1.3b) is shown in Fig. 1.4a;
2. Clusters with total demand exceeding a pre-established threshold are recursively partitioned into smaller clusters using **Algorithm 1**. The result of this step is illustrated in Fig. 1.4b. The threshold is 11 MW and is according to an informed estimate⁴ of the power rating of HV/MV substations. On the other hand, neighbour small clusters are aggregated until their total power demand reaches the threshold and so as to justify the presence of a secondary substation.
3. The location of each secondary substation is chosen at the geographical center of the convex envelope encompassing the respective aggregated cluster, as shown in Fig. 1.4c.

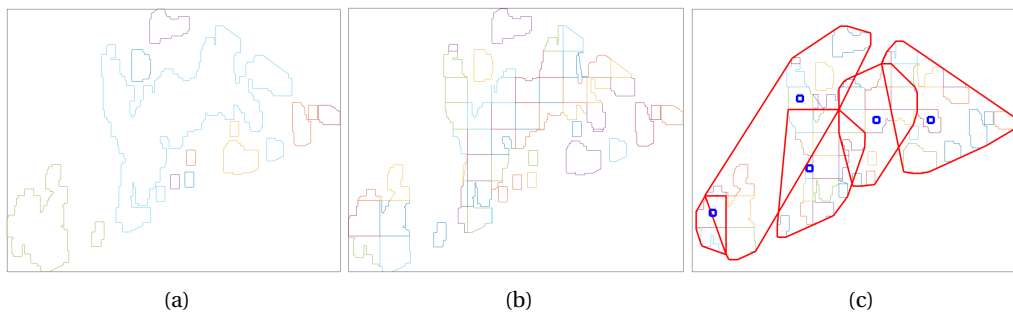


Figure 1.4: Identification of the substations locations: (a) the EHV area is divided into clusters, (b) large clusters are divided into smaller ones, (c) convex hull of the aggregated clusters (in red) and final locations of the HV substations (in blue).

Fig. 1.5a shows the distribution of the demand interfaced by the various primary substations, and the first row of Table 1.2 reports its mean and maximum value. It can be observed that, even if a static threshold of 11 MW is used to generate the clusters, the demand within each cluster is finally spread around this value. On the one hand, larger values of the total demand happen because when merging multiple clusters, their aggregated demand might exceed the threshold. On the other hand, smaller values are because certain areas have low demand.

1.3 Identification of the HV areas and MV/LV secondary substations

Once the locations of the primary substations are found, we apply the Voronoi partitioning and cluster-aggregation procedures of subsections 1.1 and 1.2.1 to identify the HV areas and the MV/LV secondary

⁴We estimate that each EHV/HV substation is connected to 5 HV/MV substations in average. The demand interfaced by each HV/MV substation is estimated as (Switzerland yearly electricity demand)/(Hours in a year)/(no of EHV substations)/5 $\approx 66 \text{ TWh}/8760/148/5 \approx 11 \text{ MW}$.

⁵Divide factor is chosen appropriately (≤ 0.5) to obtain polygons with demands smaller than L_{thres} .

Algorithm 1 Partition cluster

Require: $\text{Poly}_{\text{cluster}}$:= original cluster, L_c := cluster's total demand, demand threshold \bar{L} , μ := Divide factor ⁽⁵⁾

- 1: **if** ($L_c > \bar{L}$) **then**
- 2: $n = \text{ceil}(L/\bar{L}/\mu)$, $n_x = \text{ciel}(\sqrt{n})$, $n_y = \text{ciel}(n/n_x)$, $\tilde{n} = n_x n_y$
- 3: Find the bounding box of $\text{Poly}_{\text{cluster}}$ defined
by ($\text{Poly}_{\text{bbox}} = \{(x, y) : \underline{x} \leq x \leq \bar{x}, \underline{y} \leq y \leq \bar{y}\}$)
- 4: Partition: obtain $[\text{Poly}_{\text{div}}^1, \dots, \text{Poly}_{\text{div}}^{\tilde{n}}]$
- 5: **for** ($i = 1, \dots, n_x$) **do**
- 6: $a^i = \underline{x} + \frac{(i-1)(\bar{x}-\underline{x})}{n_x}$, $c^i = \underline{x} + \frac{(i)(\bar{x}-\underline{x})}{n_x}$,
- 7: **for** ($j = 1, \dots, n_y$) **do**
- 8: $b^j = \underline{y} + \frac{(j-1)(\bar{y}-\underline{y})}{n_y}$, $d^j = \underline{y} + \frac{(j)(\bar{y}-\underline{y})}{n_y}$
- 9: $\text{Poly}_{\text{div}}^k = \{(x, y) : a^i \leq x \leq c^i, b^j \leq y \leq d^j\}$
- 10: $\text{Poly}_{\text{div}}^k = \leftarrow \text{Poly}_{\text{cluster}} \cap \text{Poly}_{\text{div}}^k$ ▷ Intersection
- 11: $k+1 \leftarrow k$
- 12: **end for**
- 13: **end for**
- 14: Compute the demand of each small polygon: $[L_{\text{div}}^1, \dots, L_{\text{div}}^{\tilde{n}}]$
- 15: Save $[\text{Poly}_{\text{div}}^1, \dots, \text{Poly}_{\text{div}}^{\tilde{n}}]$, $[L_{\text{div}}^1, \dots, L_{\text{div}}^{\tilde{n}}]$
- 16: **end if**

substations. For the latter step, we use a threshold value for the total power within each cluster of 400 kW. This value has been chosen because it is the average power rating of the nodes of the CIGRE benchmark grid for MV european systems (C6.04.02, 2009). The distribution of the demand interfaced by the secondary substation and its statistics are reported in Fig. 1.5b and Table 1.2. Similarly to the previous case, the demand within each cluster is spread around the static threshold.

Table 1.2: Statistics on HV and MV substations

Type	Number	Mean Demand	Max Demand
HV substations	776	10.9 MW	24.7 MW
MV substations	17,844	0.41 MW	0.97 MW

Fig. 1.6a shows the identified locations of the substations for the example EHV area of Fig. 1.3b, where 5 HV/MV and 142 MV/LV substations were identified. This process is repeated for all EHV areas. The final locations of the HV and MV nodes over Switzerland are shown in Fig 1.6b, for a total of 776 and 17'844, respectively.

1.4 Routing of medium voltage networks

1.4.1 Routing algorithm

Once the locations of the MV substations are identified, we use a routing scheme to determine the connections and topologies of the corresponding grids. Several routing methods were proposed in

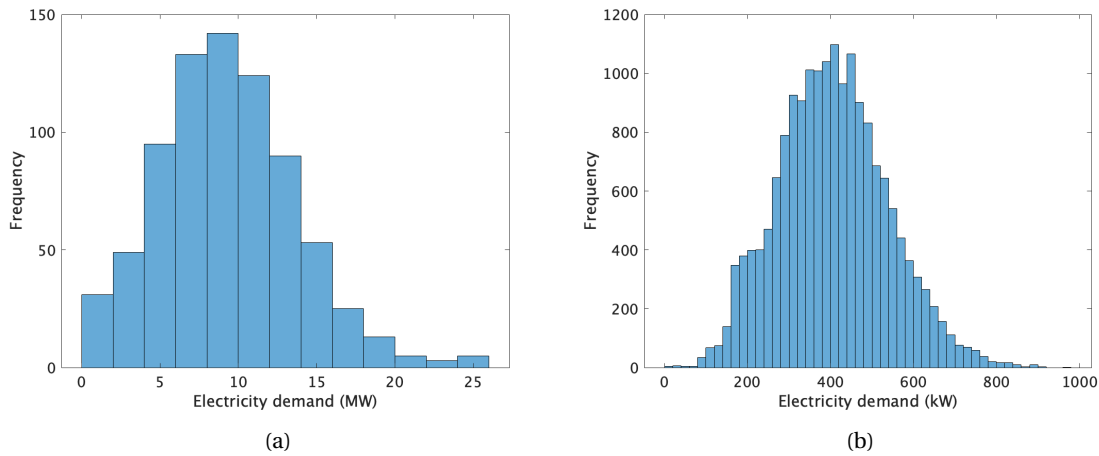


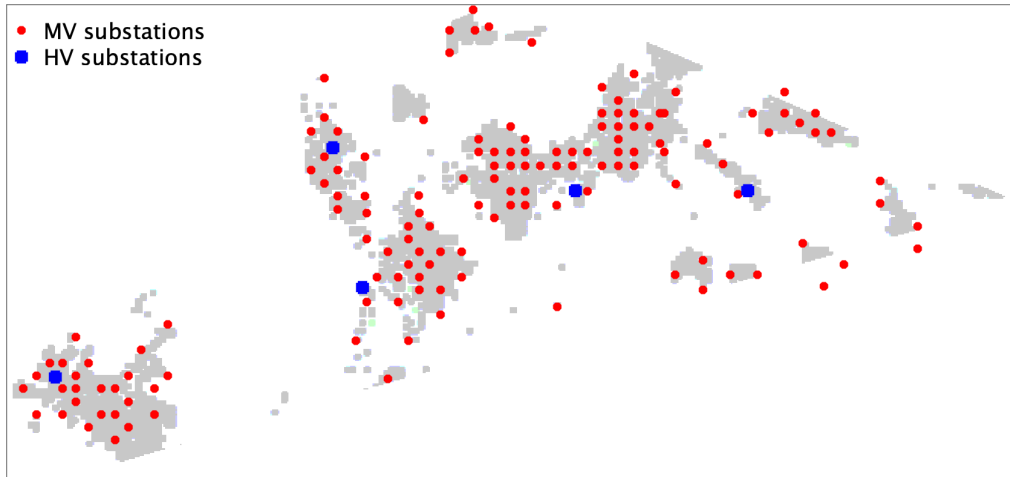
Figure 1.5: CDF plots of estimated electricity demands for (a) HV and (b) MV substations.

the literature, as discussed in the review paper (Georgilakis and Hatziaargyriou, 2015). For example, the work in Najafi et al. (2009) uses a genetic algorithm and minimum spanning tree, works in Afifi et al. (2013), Gomez et al. (2004), Diaz-Dorado et al. (2002) apply evolutionary algorithms such as simulated annealing and ant-colony. The work in Goswami (1997), Peponis and Papadopoulos (1997) proposes the branch-exchange method, and the work in Boulaxis and Papadopoulos (2002) applies dynamic programming.

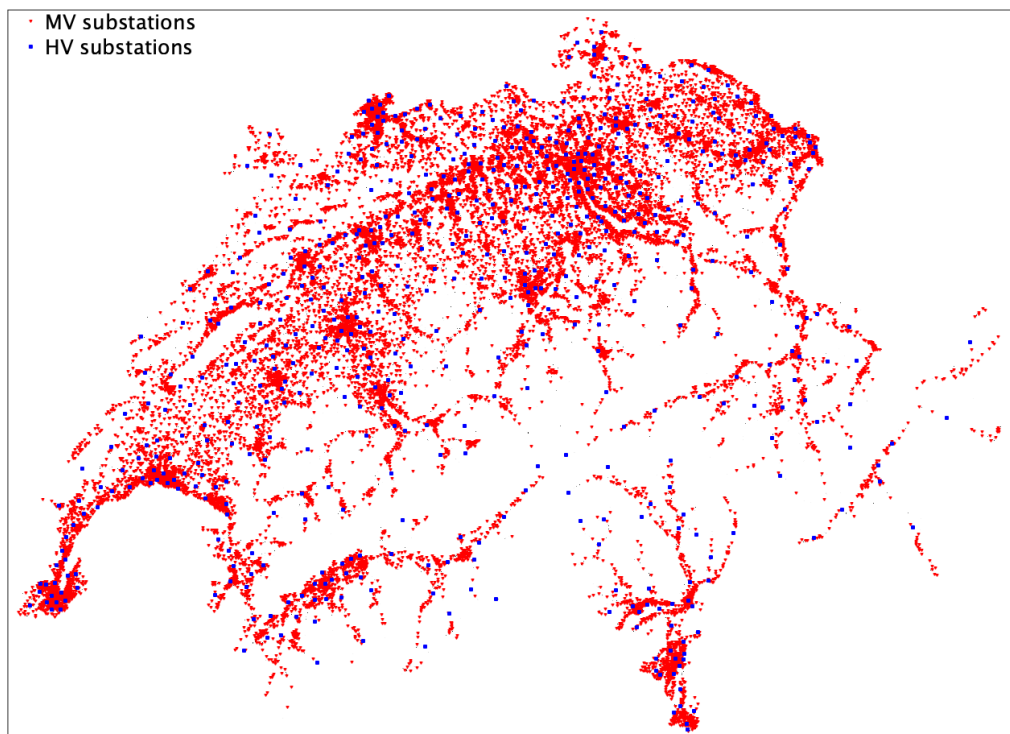
In this paper, we use the routing scheme based on the steepest gradient descent proposed in Nahman and Peric (2008), Nahman and Perić (2020) because of the faster convergence and increased tractability compared to the above-listed methods. The method accounts for the grid operational constraints on voltage magnitudes and lines ampacities. It enforces the radiality of the final system, reflecting the topology of how MV networks are normally operated. The method works by finding the grid topology that minimizes the capital cost of the grid, given by the investment cost for the power cables. In the routing scheme, we require voltage levels within a $\pm 3\%$ range of the nominal voltage (according to Swiss grid code Guide (2004)) and line currents below 80% of the respective cable ampacity, to reproduce a realistic scenario with grids operating with a safety margin on physical limits. The electrical characteristics of the lines and transformer used for the routing procedure are given in Tables 1.3 and 1.4, respectively. The rating of transformer is assumed 150 % of the total nominal demand to reflect a planning scenario where operators allow equipments to operate with a safety margin from their maximum ratings.

The routing scheme starts from a base topology where each substation node is connected to the 6 nearest ones (a value inspired from the work in Wang et al. (2010) depicting an upper bound on the connections to/from a node in a typical power grid). Then, the following steps are performed:

1. run the routing scheme in **Algorithm 2** by selecting high-ampacity type-4 cables (from Table 1.3) for all the lines;
2. replace the type-4 cables (since they are most expensive ones according to their ampacity) with ones with lower ampacity according to the criterion reported in Table 1.5. For example, if the maximum line current in the first-stage routing is less than 10 % of the type-4 cable's ampacity, it is replaced with a type-1 cable. Once each single cable is replaced, we perform a load flow to



(a)



(b)

Figure 1.6: Identified HV and MV substations for (a) the example EHV area (5 and 142, respectively) and (b) the whole country (776 and 17'844)

verify voltage and current conditions and, if they are not satisfied, the original cable is restored.

Table 1.3: Cable ratings from a commercial source.

Cable Type	Section [mm ²]	Resistance [Ohm/km]	Reactance [Ohm/km]	Capacitance [μ F/km]	Ampacity [A]
1	50	0.495	0.13	0.19	228
2	70	0.344	0.13	0.21	284
3	95	0.248	0.12	0.23	346
4	120	0.198	0.12	0.25	399

Table 1.4: Transformer rating (C6.04.02, 2009).

HV voltage [kV]	MV voltage [kV]	Short-circuit impedance [Ohms]	Power rating [MVA]
110	20	0.016 + j1.92	25

Algorithm 2 Routing

Require: Base topology, line parameters, lines set

- 1: **while** Routing is successful (the network is connected and feasible) **do**
 - 2: Remove the most expensive line (by length) from the lines set
 - 3: Proceed to step 4 if connected else go to step 7
 - 4: Compute admittance matrix, perform load flow, proceed to step 5 if converged else go to step 7
 - 5: Proceed to step 6 if the voltage and currents are within bounds else go to 7
 - 6: Save the network, update the lines set and go to step 2
 - 7: Keep the previous network, remove this line from the lines set, go to step 2.
 - 8: **end while**
-

Figure 1.7 shows the step-by-step routing results for an example EHV area. Fig. 1.7b shows the initial routing, which is obtained by connecting each node with the nearest 6 nodes. Fig 1.7c shows an intermediate stage of the routing, where some of the redundant lines have been removed. The final topology is shown in Fig. 1.7d, where the color of the lines denotes their ampacities. Fig. 1.7e shows the evolution of the capital cost of the grid at each routing iteration. The cost decreases with the number of iterations and settles after 300 iterations. In this example, the initial and final iterations correspond to 67 km and 10.5 km, respectively, of deployed lines.

1.4.2 Re-routing unsuccessful networks

In certain cases, the routing by **algorithm 2** might fail. This happens when a subset of the nodes in the given region is very distant in space to the rest of the nodes requiring very long cables. It either results in violations on voltage and currents or convergence issues while solving load-flows or requires a meshed topology with single or multiple rings to be feasible. These networks are labelled

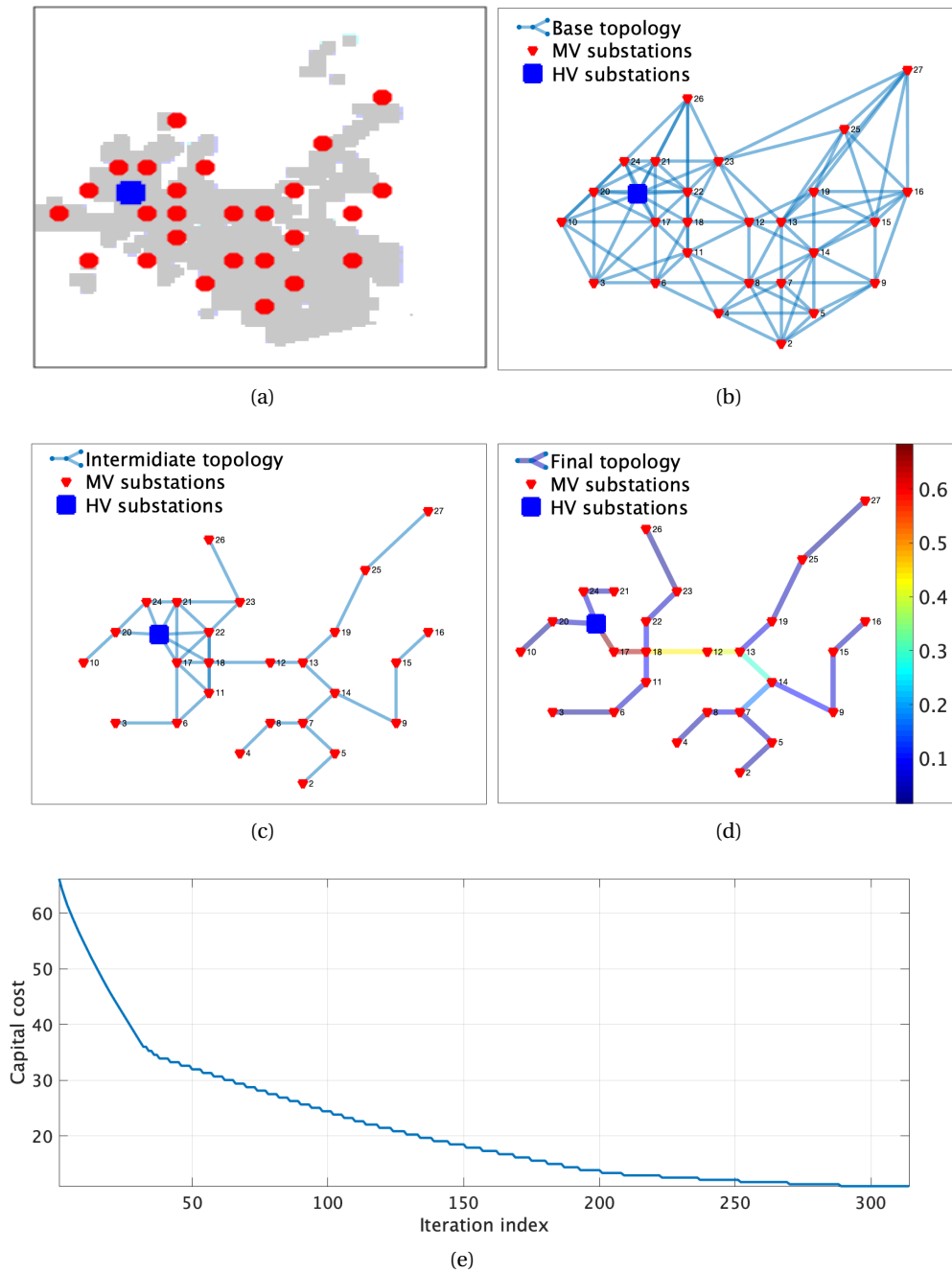


Figure 1.7: Routing procedure:(a) example EHV area with HV and MV substations, (b) highly-connected base topology, (c) meshed grid topology at an intermediate stage of the procedure, (d) final topology highlighting the current levels in the cables, and (e) total capital cost (expressed in km for length of cables used) as a function of the iteration.

Table 1.5: Replacement scheme for lines.

Current range (pu)	Cable type
$0 < 0.1$	1
$0.1 \leq 0.2$	2
$0.2 \leq 0.4$	3

as *unsuccessful* networks. To solve this issue, we propose a re-routing procedure, where we divide the region further using a clustering method. The steps are described in **algorithm 3**. An example is shown in Fig. 1.8, where on the left figure, we see a meshed network to enable it to be routed due to current and voltage violations, whereas the right figure shows that the network is divided into two separate radial networks.

Algorithm 3 Re-routing

Require: Substations' geographical locations

- 1: **while** The network is connected and feasible **do**
- 2: Split the *unsuccessful* networks into two areas using *k-means* clustering with locations as features
- 3: Place HV substations at the centroid of two areas, re-route both the areas using **algorithm 2**
- 4: Proceed to step 5 if network routing is successful else go to 2
- 5: Save the networks.
- 6: **end while**

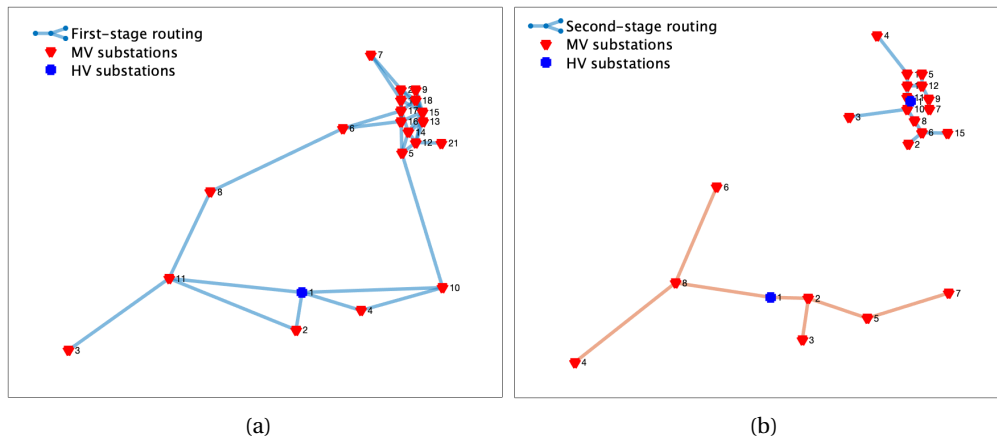


Figure 1.8: Re-routing: (a) routed network using algorithm 1 resulting in a meshed network, (b) routed network using algorithm 2 which divides it into two radial networks.

The final routing results for the example EHV region is shown in Fig. 1.9. Statistics on the routed networks for the whole Switzerland are listed in the Table 1.6. The distributions of the nodal voltages and the lines currents are shown in Fig. 1.10 and denote that design requirements are met.

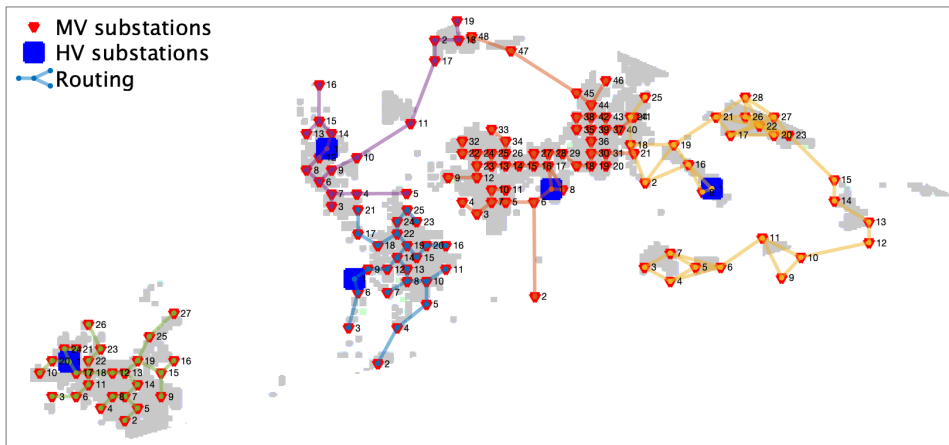


Figure 1.9: Routed MV networks for the example EHV area.

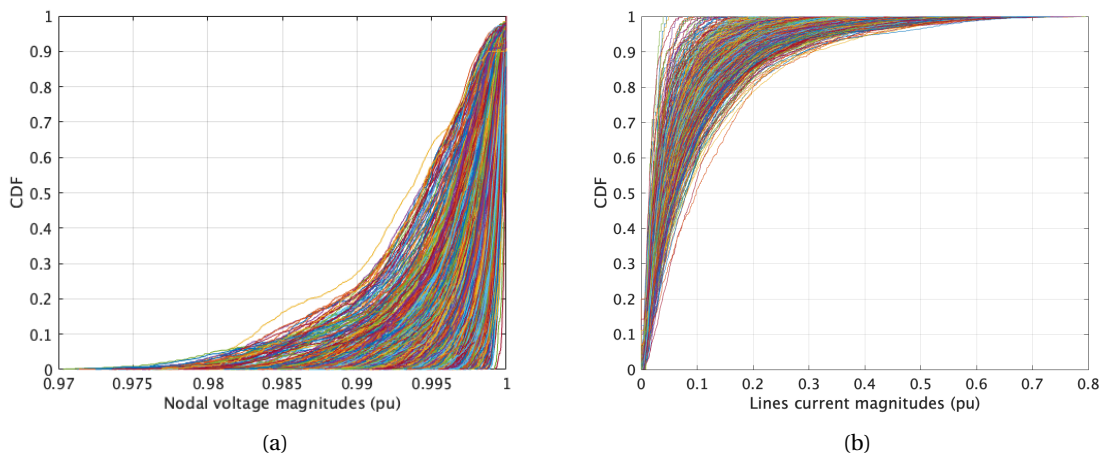


Figure 1.10: CDF plots (a) nodal voltages and (b) lines currents of estimated networks shown in different colors.

Table 1.6: Number of identified grid components.

Equipment	Number of elements
HV-MV transformers	776
MV-LV transformers	17'844 x 2 (for redundancy)
MV cables and overhead lines	1342.2 km

Chapter 2

PV hosting capacity and energy storage requirements

The PV hosting capacity of a distribution grid is the maximum amount of PV generation that the grid can accommodate without violations of its operational constraints. In this section, we describe the PV hosting capacity problem for distribution grids and, then, how to increase it with distributed energy storage systems (Nick et al., 2017). Other options such as grid-reinforcements and curtailment of PV generations are not considered in this work. Finally, we discuss the optimal deployment of PV power plants and BESSs to achieve the largest production at the minimum cost for the whole country. We first discuss the input data that are used in the problem formulation.

2.1 Input data

2.1.1 Capacity factor of PV production

PV capacity factors (total actual generation to the total generation at the nominal plant capacity over one year) for all locations across the country are used to compare the suitability for hosting PV generation. Capacity factors are from PVGIS estimations considering optimal panel locations (south-facing and 38° tilt for the case of Switzerland). They are based on satellite information at a 3x3 km (at Nadir) resolution and are corrected for the shading induced by topographical features on the horizon. We query this information for the whole Switzerland with a resolution of 1.5x1.5 km. Figure 2.2a shows the distribution of the capacity factors across the country. It denotes variable values that can vary up to a factor of 3.

2.1.2 Land-use constraints for PV generation

We evaluate land allocation to identify suitable locations for PV power plants. We use a 100x100 m resolution land-use map¹ from the Swiss Federal Office for Topography, shown in Fig. 2.1, reporting settlement (residential, commercial, industrial and recreational) and agricultural areas. For the area corresponding to each MV grid, we consider that 10% of the settlement areas can host PV generation, for a total surface of 210 km² for the whole country. Considering this available surface, the

¹<https://map.geo.admin.ch/?layers=ch.bfs.arealstatistik-hintergrund&lang=en&topic=ech&bgLayer=ch.swisstopo.pixelkarte-farbe>

Table 2.1: A comparison of the PV generation potential.

Reference	Area [km ²]	Estimated PV generation [TWh]
Assouline et al. (2017)	328	17.86
Assouline et al. (2018)	252	16.29
Buffat et al. (2018)	485	41.32
Walch et al. (2020)	267	24 ± 9
This work	210	33

yearly capacity factors from PVGIS, and an average PV conversion efficiency of 15 % in standard conditions (Walch et al., 2019), the yearly total PV generation for Switzerland with these assumption is of 33 TWh. Both the available area for PV deployment and total generation are in-line with the estimates reported in the existing literature (Assouline et al., 2017, 2018, Buffat et al., 2018, Walch et al., 2020) as summarized in Table 2.1. Differences among the various estimations (more remarkably for PV generation) can be explained by different input data sets and methods, however they all seem to agree on the same order of magnitude. Fig. 2.2b shows the distribution of the PV installed capacity potential (solely based on land availability) across all the MV grids of the country. Its mean and maximum values are 2 and 13.1 MW. The total PV installed capacity potential with the above assumptions is of 30 GW. It is worth noting that larger capacity values are possible with higher usage of available land and PV conversion efficiency.

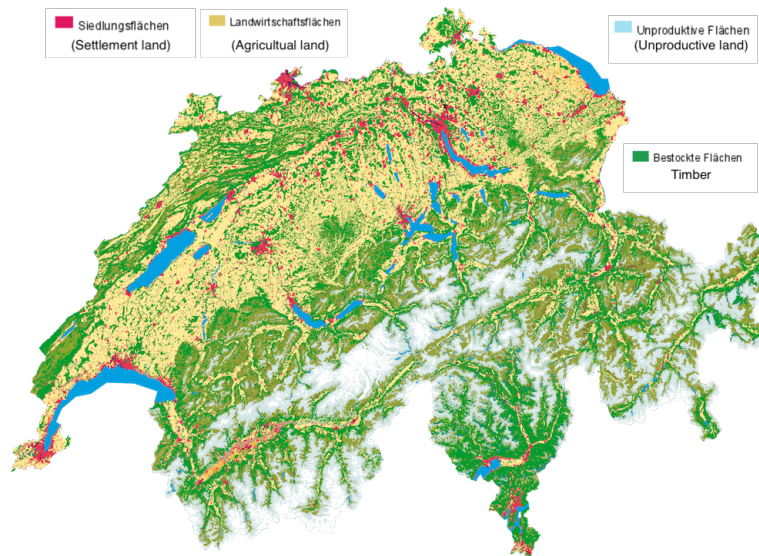


Figure 2.1: Simplified land-use map of Switzerland.

2.1.3 Time series of the PV generation and demand

Solving the PV hosting capacity problem does require time series of PV generation and demand to model the loading conditions of the grid. We consider a scenario with high PV generation and low demand to reproduce cases where excess PV generation might cause violations of the grid constraints. In this respect, PV generation is modelled considering uniform clear-sky conditions over the whole power distribution network and considering the day of the year with the largest PV generation. We

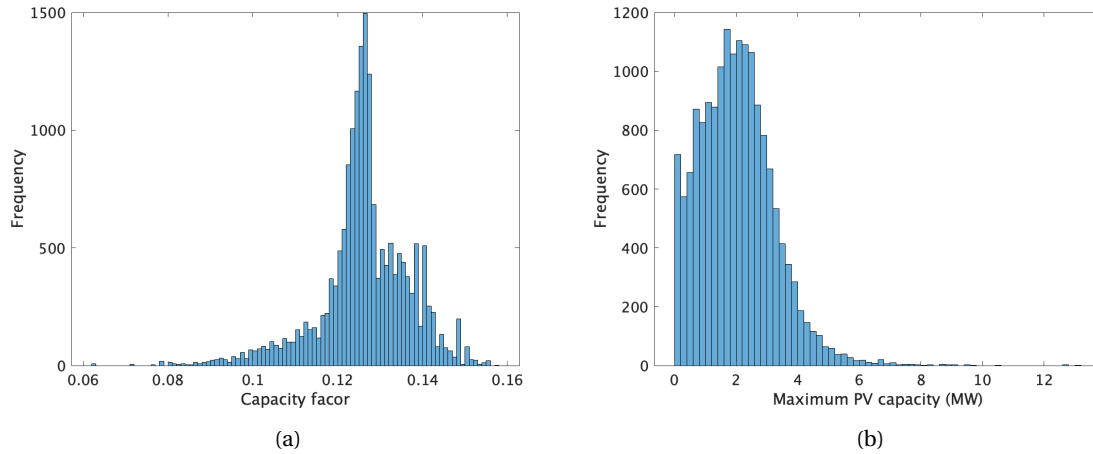


Figure 2.2: Distribution of (a) capacity factor and (b) maximum PV capacity per MV node due to land constraint.

use a clear-sky model to compute the global-horizontal irradiance (GHI) as a function of the location, that we denote by n . The plane-of-array (POA) irradiance $I_{t,n}$ (kW/m^2) is determined by transposing the GHI as a function of the plant tilt and azimuth, and time of the day. The POA irradiance is finally converted to PV generation for a plant with P^{PV} capacity (in kW) with the following model $g(t, n, P^{\text{PV}})$:

$$p_{t,n}^{\text{PV}} = g(t, n, P^{\text{PV}}) = I_{t,n} (1 + \alpha(T_{t,n}^{\text{air}} + \beta I_{t,n} - 25)) P^{\text{PV}} \quad (2.1)$$

where T_t^{air} is the air temperature ($^{\circ}\text{C}$), $\alpha = -0.0043$ and $\beta = 0.038$ are empirical parameters as in Sossan et al. (2019) for open-rack PV plants.

Demand profiles are obtained by scaling the residential, commercial and industrial demand profiles specified in the CIGRE benchmark grid for MV systems (C6.04.02, 2009), shown in Fig. 2.3a, for the coefficients extracted from the demand map computed in subsection 1.2. To reproduce a scenarios with dominant PV generation over the demand, we halve the nominal demand profile to reflect a day with low electricity consumption. We assume ideal correlation among the loads. Being the focus of the paper on modeling the impact of PV generation on the grid hosting capacity, modeling spatial diversity of the loads is not of special interest. We consider voltage- and frequency-independent loads. Figure 2.3b shows the PV and the load profiles considered for the PV and battery sizing.

2.2 The PV hosting capacity problem

The objective of this problem is determining the maximum PV installed capacity that a grid can host at its nodes without violations of grid constraints. We consider a generic distribution grid with N_{bus} nodes and L lines with index $n \in \mathcal{N} = \{1, \dots, N_{\text{bus}}\}$ and $l \in \mathcal{L} = \{1, \dots, L\}$, respectively. The installed PV capacity at node n , that is an unknown of the problem, is denoted by P_n^{PV} (²). As discussed in Section 2.1.2, the installed capacity is limited by the land availability, so we say that $P_n^{\text{PV}} \leq \overline{P}_n^{\text{PV}}$,

²For generality, if a node cannot host PV generation, we can add in the following formulation a constraint of the kind $P_n^{\text{PV}} = 0$.

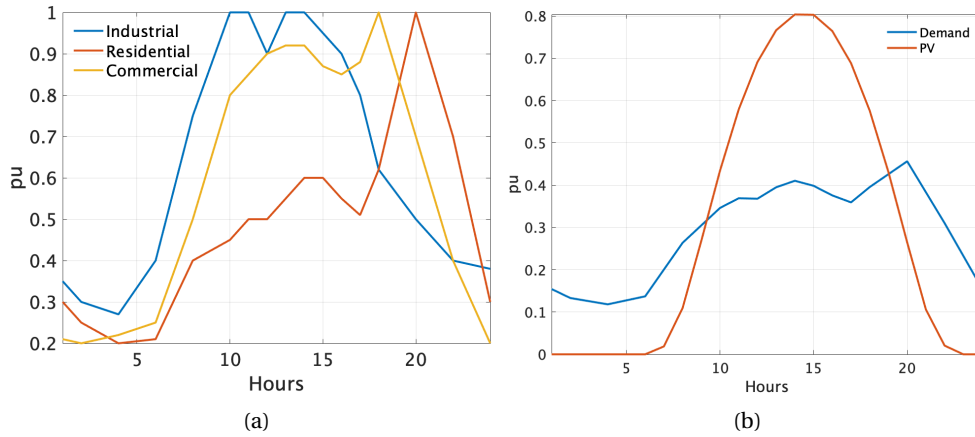


Figure 2.3: Demand and PV scenarios: (a) standard load profiles for different sector from (C6.04.02, 2009), (b) scenario considered for the PV and battery sizing problem.

where the right-hand-side upper-bound is derived from the land availability map. Active and reactive nodal injections at the various nodes of the grid are collected in the bold-typeface vectors $\mathbf{p}_t, \mathbf{q}_t$. They are given by the difference between the nodal PV generation $\mathbf{p}_t^{\text{PV}}, \mathbf{q}_t^{\text{PV}}$ (if available) and demand $\mathbf{p}_t^{\text{load}}, \mathbf{q}_t^{\text{load}}$. We assume that PV plants operates at unitary power factor, so $\mathbf{q}_t^{\text{PV}} = \mathbf{0}$ (as usually done for small/medium size PV plants connected to power distribution systems). PV generation is given by applying the model $g(\cdot)$ in (2.1). Vectors \mathbf{v}_t and \mathbf{i}_t collect nodal voltage and line current magnitudes, respectively. They, and the corresponding complex power at the grid connection point, are modelled as a linear function of the nodal injections and the voltage at the slack bus with a model based on sensitivity coefficients and described in A. In the following, we denote the voltage and current linear model with the general notation $\mathbf{v}_t = \nu(\mathbf{p}_t, \mathbf{q}_t, \mathbf{v}_0)$ and $\mathbf{i}_t = c(\mathbf{p}_t, \mathbf{q}_t, \mathbf{i}_0)$, where $\mathbf{v}_0, \mathbf{i}_0$ are the initial operating point for power-flow linearization (see A). Voltage magnitudes and line currents should be within allowed voltage limits, denoted by $\underline{\mathbf{v}}, \bar{\mathbf{v}}$, and respect cable ampacities $\bar{\mathbf{i}}$. Similarly, the apparent power at the substation transformer is denoted by the model $s(\mathbf{p}_t, \mathbf{q}_t, \tilde{s}_0)$ and should be less than substation transformer rating \bar{S} , where \tilde{s}_0 is the operating complex apparent power used for the power-flow linearization.

The problem consists in maximizing the installed capacity of PV generation while subject to grid constraints. To foster the deployment of the PV plants in nodes with the highest irradiance availability, the installed capacity is weighted by the local capacity factor γ_n ³. The problem formulation is:

$$\underset{\{P_n^{\text{PV}} \in \mathbf{R}^+, n \in \mathcal{N}\}}{\text{maximize}} \left\{ \sum_{n \in \mathcal{N}} \gamma_n P_n^{\text{PV}} \right\} \quad (2.2a)$$

³We include the capacity factor because, even if derived from satellite estimations with coarser resolution than the grid nodes, the topographical shading is at a higher resolution and could impact on the suitability of certain nodes.

subject to nodal injections model and grid constraints

$$\mathbf{p}_t = \mathbf{p}_t^{\text{pv}} - \mathbf{p}_t^{\text{load}} \quad t \in \mathcal{T} \quad (2.2b)$$

$$\mathbf{q}_t = \mathbf{p}_t^{\text{pv}} - \mathbf{q}_t^{\text{load}} \quad t \in \mathcal{T} \quad (2.2c)$$

$$\underline{\mathbf{v}} \leq \nu(\mathbf{p}_t, \mathbf{q}_t, \mathbf{v}_0) \leq \bar{\mathbf{v}} \quad t \in \mathcal{T} \quad (2.2d)$$

$$\mathbf{0} \leq c(\mathbf{p}_t, \mathbf{q}_t, \mathbf{i}_0) \leq \bar{\mathbf{i}} \quad t \in \mathcal{T}, \quad (2.2e)$$

$$0 \leq s(\mathbf{p}_t, \mathbf{q}_t, \tilde{s}_0) \leq \bar{S} \quad t \in \mathcal{T}, \quad (2.2f)$$

and PV generation model and land-availability constraint $\overline{P_n^{\text{pv}}}$:

$$p_{n,t}^{\text{pv}} = g(t, n, P_n^{\text{pv}}) \quad t \in \mathcal{T}, n \in \mathcal{N} \quad (2.2g)$$

$$P_n^{\text{pv}} \leq \overline{P_n^{\text{pv}}} \quad n \in \mathcal{N}. \quad (2.2h)$$

2.3 Increasing PV hosting capacity with BESSs

Problem formulation

The objective of this problem is to determine the optimal location of PV plants to host a target level of total PV generation capacity, that we denote by P^* . However, values of P^* above the grid's PV hosting capacity cannot be accommodated because they would lead to violations of grid constraints. For this reason, this problem also determines an optimal configuration of BESSs (location, converter power ratings, and energy capacities) to relieve grid constraints and enabling the further integration of PV generation in the grid. The results of this process are discussed at the end of this section.

It is worth highlighting that, even if we consider BESSs, the formulation can be extended to other forms of energy storage systems or other resources capable of providing grid support, like flexible demand (Sossan, 2017, Fabietti et al., 2018). It is also worth highlighting the parallel with PV self-consumption strategies, which can indirectly mitigate the impact of excess PV generation on grid constraints thanks to promoting the direct consumption of locally generated electricity, see e.g. Sossan et al. (2013), Luthander et al. (2015). PV self-consumption is typically provided on a best-effort basis by end consumers and is typically unaware of global grid conditions, thus without offering reliable performance guarantees. Compared to PV self-consumption, we provide robust guarantees on grid control performance and optimized energy storage requirements considering the whole grid and not a single consumer.

BESSs model BESSs' active power is denoted by $p_{n,t}^{\text{bess}}$, and reactive by $q_{n,t}^{\text{bess}}$. We model the evolution of the BESS state-of-energy (SOE) with

$$\text{SOE}_{n,t} = \text{SOE}_{n,t-1} - p_{n,t}^{\text{bess}} \Delta t, \quad (2.3)$$

where Δt is the sampling time. Charging and discharging efficiency is accounted for by integrating the BESS equivalent resistance in the load flow problem as proposed in Stai et al. (2020). If load flow equations are linearized, this modeling choice retains the convexity of the problem without requiring

the use of additional variables as, for example, in Kraning et al. (2011). Since battery sizes are the decision variables, the optimization problem is solved multiple times taking account of the updated equivalent resistances in proportion to their converter ratings. To implement a safety margin from zero-SOE and full charge, we implement the following constraint

$$aE_n^{\text{bess}} \leq \text{SOE}_{n,t} \leq (1-a)E_n^{\text{bess}} \quad (2.4)$$

where $0 \leq a \leq 0.5$ is a design parameter and E_n^{bess} is the BESS energy capacity. BESS injections should respect the capability curve of its four quadrant power converter. This reads as:

$$0 \leq (p_{n,t}^{\text{bess}})^2 + (q_{n,t}^{\text{bess}})^2 \leq (P_n^{\text{bess}})^2. \quad (2.5)$$

Capital investment for BESSs and PV plants The capital investment for installing a PV plant with generation capacity P^{PV} , and a BESS with energy capacity E_n^b and power rating P_n^b at node n is:

$$J(P_n^{\text{PV}}, P_n^{\text{bess}}, E_n^{\text{bess}}) = \mathcal{C}_n^{\text{PV}} P_n^{\text{PV}} + \mathcal{C}^P P_n^{\text{bess}} + \mathcal{C}^E E_n^{\text{bess}}, \quad (2.6)$$

where \mathcal{C}^{PV} , \mathcal{C}^P , and \mathcal{C}^E are the unitary costs for PV, power converter rating, and energy capacity, respectively. Costs are reported in Table 2.2. They are derived from current market figures.

Table 2.2: Costs of PV and BESSs.

Component	Unit	Value
Turn-key PV system (\mathcal{C}^{PV})	USD(\$)/kWp	1020
BESS converter rating (\mathcal{C}^P)	USD(\$)/kVA	200
BESS energy capacity (\mathcal{C}^E)	USD(\$)/kWh	300

Formulation of the decision problem The decision variables of the problem are the installed PV capacity, the BESS power rating and the BESS energy capacity at all the nodes of the grid, which we collect in the set $\chi = \{P_n^{\text{PV}}, P_n^{\text{bess}}, E_n^{\text{bess}} \in \mathbf{R}^+, \forall n \in \mathcal{N}\}$. Without losing generality, nodes that cannot host PV generation or BESS can be excluded by properly subsetting the nodes index. The problem consists in locating and sizing BESS to accommodate a target level P^* of installed PV generation capacity while minimizing the total capital investment (2.6) for all the nodes of the grid. Similarly to before, to penalize location with large PV capacity factors, we weight the installed PV capacity at each node with the factor $\bar{\gamma}/\gamma_n$, where $\bar{\gamma}$ is the average among all the capacity factors $\gamma_n, n \in \mathcal{N}$ in the network. Finally, the problem is:

$$\underset{\chi}{\text{minimize}} \left\{ \sum_{n \in \mathcal{N}} J\left(\bar{\gamma}/\gamma_n \cdot P_n^{\text{PV}}, P_n^{\text{bess}}, E_n^{\text{bess}}\right) \right\} \quad (2.7a)$$

subject to nodal injections (now with BESSs demand too) and grid constraints

$$\mathbf{p}_t = \mathbf{p}_t^{\text{pv}} - \mathbf{p}_t^{\text{load}} - \mathbf{p}_t^{\text{bess}} \quad t \in \mathcal{T} \quad (2.7b)$$

$$\mathbf{q}_t = \mathbf{p}_t^{\text{pv}} - \mathbf{q}_t^{\text{load}} - \mathbf{q}_t^{\text{bess}} \quad t \in \mathcal{T} \quad (2.7c)$$

$$(2.2d) - (2.2f), \quad (2.7d)$$

BESS model and constraints

$$\text{SOE}_{n,t} = \text{SOE}_{n,t-1} - p_{n,t}^{\text{bess}} \Delta t \quad t \in \mathcal{T}, n \in \mathcal{N} \quad (2.7e)$$

$$0 \leq (p_{n,t}^{\text{bess}})^2 + (q_{n,t}^{\text{bess}})^2 \leq (P_n^{\text{bess}})^2 \quad t \in \mathcal{T}, n \in \mathcal{N} \quad (2.7f)$$

$$aE_n^{\text{bess}} \leq \text{SOE}_{n,t} \leq (1-a)E_n^{\text{bess}} \quad t \in \mathcal{T}, n \in \mathcal{N} \quad (2.7g)$$

and PV model and target PV capacity P^* to install in the grid:

$$(2.2g) - (2.2h) \quad (2.7h)$$

$$\sum_{n \in \mathcal{N}} P_n^{\text{pv}} = P^*. \quad (2.7i)$$

2.3.1 Results

For each estimated MV grid, first, we solve the PV problem (2.2) to obtain the PV hosting capacity, then, we solve the BESS sizing problem (2.7) by varying P^* in (2.7i) from 25% to 300% (with increments of 25%) of the grid PV hosting capacity. It should be noted that both the problems (2.2) and (2.7) are solved multiple times for correcting the grid linearization (by updating the injections of newly sized PV and battery installations) and updating battery equivalent resistances (for the battery loss model as previously mentioned). With this procedure, we determine the BESSs requirements for PV configurations below (25-100%) and above (125-300%) the grid hosting capacity. The results of this process for are shown in Fig. 2.4 and are now discussed. Figures 2.4a and 2.4b show the cost curves for 10 randomly chosen distribution networks, whereas Figures 2.4c and 2.4d show the distribution along the grids with symmetric quantiles. Figure 2.4a shows the total investment for PV systems and BESSs as a function of the installed PV generation capacity. We can observe two elements. Networks reach a different level of maximum PV installed capacity. This is due to the different values of land availability. Second, the total investment grows at two different rates because the investment, below the hosting capacity, is given by PV panels only, whereas above it, by BESSs too. Figure 2.4b shows the marginal cost of increasing the level of installed PV generation capacity. We define the marginal cost of each grid as the cost of the system over the total PV yearly production over one year accounting for the capacity factor:

$$\text{Marginal cost} = \sum_{n \in \mathcal{N}} \frac{J(\hat{P}_n^{\text{pv}}, \hat{P}_n^{\text{bess}}, \hat{E}_n^{\text{bess}})}{\hat{P}_n^{\text{pv}} \cdot 365 \cdot 24 \cdot \gamma_n}, \quad (2.8)$$

where $\hat{P}_n^{\text{pv}}, \hat{P}_n^{\text{bess}}, \hat{E}_n^{\text{bess}}$ denote the solution of problem (2.7). It can be seen from Fig. 2.4a and 2.4b that below the hosting capacity, the marginal cost is constant because it corresponds to the unitary cost of PV, whereas above it, the marginal cost increases because progressively larger BESSs are required. Figure 2.4c and 2.4d shows the density plot of the cost curves derived for all estimated MV networks in Switzerland.

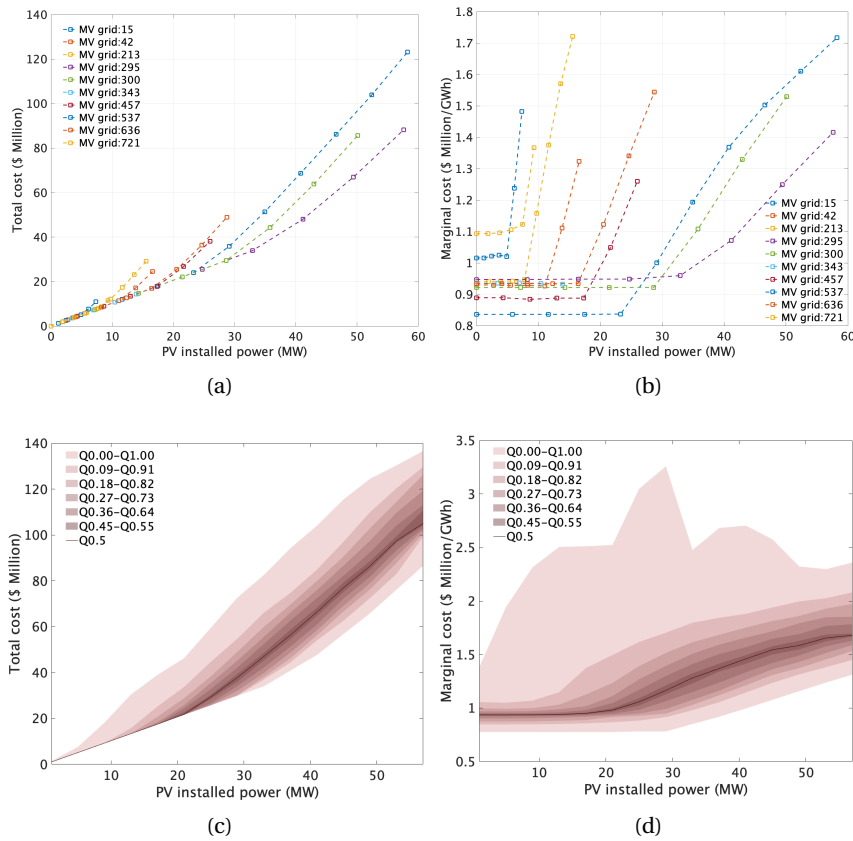


Figure 2.4: Investments to achieve a target level of installed PV generation capacity: (a, c) total cost, and (b, d) marginal cost. Top: for randomly chosen 10 MV networks, bottom: for all estimated MV networks in Switzerland (distribution with symmetric quantiles).

2.4 Optimal allocation of PV and BESSs

In the former subsection, we have discussed a method to determine the optimal deployment of PV installations and BESSs within a network to accommodate a target level of installed PV capacity. We have applied it to all identified grids of Section 2 and derived, for each of them, marginal costs for installing increasing levels of installed PV capacity. The estimated marginal costs are key results as they allow us to compare the costs of installing PV generation in various networks across the country, and they will be the fundamental input of the problem discussed in this section. The objective of this problem is to determine the installed PV capacity in each network in order to achieve a country-wide objective for total PV generation at the lowest capital cost.

We denote the curves of Fig. 2.4b with the function $f_m(P_m^*)$, where $m \in \mathcal{M} = \{1, \dots, M\}$ is the index for the identified MV networks and P_m^* is the installed capacity in grid m . We approximate the curves f_m with a piece-wise linear function. The domain of f_m is $[\underline{P}_m^*, \bar{P}_m^*]$, derived from Fig. 2.4b. The problem consists in finding the variables P_1^*, \dots, P_M^* at the minimum total cost and such that the total installed capacity equals the country-wide PV installation target P^{target} . The problem is:

$$\underset{\{P_m^* \in \mathbf{R}^+, m \in \mathcal{M}\}}{\text{minimize}} \left\{ \sum_{m \in \mathcal{M}} \mathcal{P}_m^{\text{PV}} f_m(\mathcal{P}_m^{\text{PV}}) \right\} \quad (2.9a)$$

subject to the domains of the variables and the PV installation target:

$$\underline{P}_m^* \leq P_m^* \leq \overline{P}_m^* \quad m \in \mathcal{M} \quad (2.9b)$$

$$\sum_{m \in \mathcal{M}} P_m^* = P^{\text{target}}. \quad (2.9c)$$

The results are discussed in the next section.

Chapter 3

Results and Discussion

3.1 Case study

In the previous sections, we have presented a modeling toolchain that determines an economically optimal deployment of PV plants and BESSs to achieve a target level of installed PV generation while accounting for the capacity factor spatial distribution, grids constraints and how they can be relieved by BESSs when the PV generation capacity exceeds the grid's PV hosting capacity. It is worth highlighting that the problem's essence is not only about achieving an optimal deployment of PV generation based on its country-wide potential but also extending with distributed energy storage the PV hosting capacity of grids with large PV generation potential if this leads to more economically convenient configurations. For example, as shown in this section, it is more convenient to invest in BESSs to extend the hosting capacity of a grid with a large generation potential and installing here additional PV generation rather than in grids with lower generation potential to avoid installing BESS.

In this section, we compare this approach (that we call **Case 1**) against the case where the same level of installed PV generation capacity is deployed uniformly in the distribution grids (**Case 0**). For an illustrative comparison between Case 0 and 1, we refer to Fig. 2.4d: for a given value of total PV generation capacity, Case 0 involves selecting, for each network, an installed PV generation capacity (x-axis) that is proportional to the grid area and regardless of its cost (y-axis). Case 1 involves placing PV generation starting from the grid with the lowest cost (y-axis), and saturating its potential (sweeping the x-axis) before moving to the second cheapest grid.

3.2 Deployment of PV plants

Figure 3.1 shows the distribution of installed PV generation capacity across Switzerland for increasing (from top to bottom) levels of total installed capacity and for Case 0 (left column) and Case 1 (right). The difference between the two deployment policies is evident by comparing the plots in the first row: in the left plot (Case 0), PV plants are installed uniformly in the grids¹, whereas in the right plot (Case 1) PV is installed prioritizing regions with higher irradiance availability, which appear to be Ticino, Lemman and Neuchatel regions, and west Valais.

For increasing values of installed PV capacity (second and third rows of Fig. 3.1), it can be observed that Case 0 and Case 1 feature increasingly similar geographical distribution patterns. This is due to

¹Non-uniform spatial distribution over the country of PV generation is because grids are not uniformly distributed.

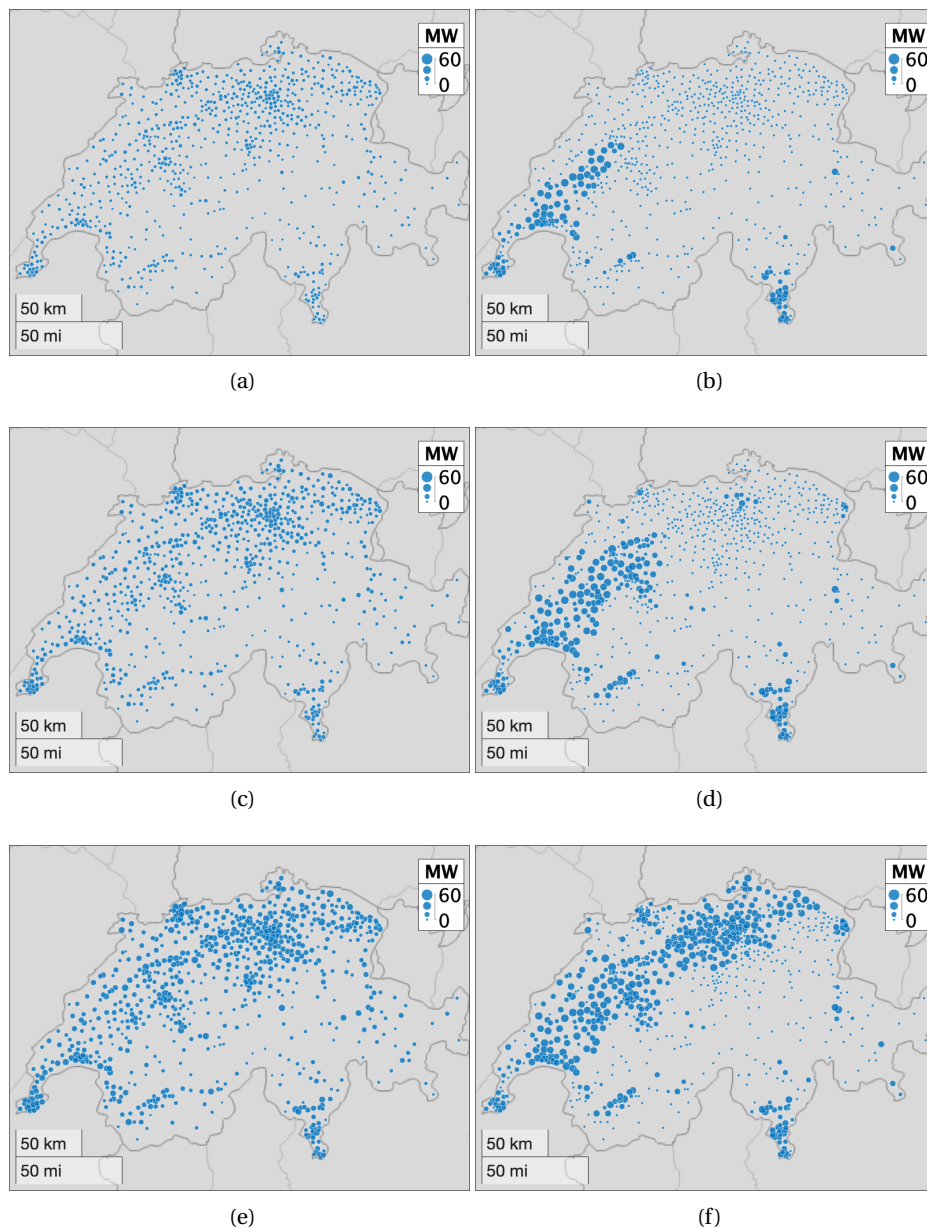


Figure 3.1: Installed PV generation capacity (in MW) across Switzerland for scenario A in (a) and (b), scenario B in (c) and (d), and scenario C in (e) and (f), for Case 0 and Case 1, respectively. Scenarios refer to the installed capacity of PV generation and are defined in Table 3.1.

land-use limitations, and the activation of the associated constraint in (2.2h). In other words, once Case 1 saturates the available locations for PV deployment in regions with high irradiance potential, it starts installing PV generation in second-choice grids. The distribution of the BESS follows the same pattern as of PV.

3.3 Deployment of PV plants and BESSs for Case 0 and Case 1

Table 3.1 shows the PV installed capacity, the yearly production, the BESS power rating and energy capacity, and the total cost (i.e., investments for PV plants and BESSs) for 10 scenarios (A-J) of PV generation deployment for Case 0 and Case 1. Scenarios A, B, C to J correspond to allocating PV generation in 5, 10, 20 to 90% (with increments of 10%), respectively, of the available surface. We remind that the available surface for PV is 10% of the settlement areas, as discussed in section 2.1.2. The energy transition scenario for Switzerland reported in Bauer and Hirschberg (2017) estimates a yearly PV production potential from roof-top PV around 25 TWh, that corresponds to our scenarios H-J.

From Table 3.1 we can make the following observations.

- Case 1/Scenario A achieves a 0.21 TWh increase in yearly production compared to the same scenario of Case 0 thanks to installing PV generation in distribution grids with larger PV generation potential first. For increasing values of installed capacity (scenarios from B to J), the yearly production of the two cases converges to the same values due to land-use limitations, as discussed in 3.2;
- Case 0 requires BESSs starting from Scenario C, whereas Case 1 has mild needs in Scenario B already. This denotes that it is more cost effective to invest in BESS to increase the hosting capacity of high PV-generation-potential grids rather than connecting that same PV capacity in other grids with less PV generation potential.
- Connecting PV generation above Scenario C in Case 0 requires progressively larger values of energy storage capacity and power rating. For example, doubling its installed capacity (from 6.85 to 13.75 GW) requires nearly 40 times the energy storage capacity (from 0.14 to 5.73 GWh). It is worth noting that the needs for BESSs increases sharper for Case 0 than Case 1. This is because the latter problem optimizes the locations of BESSs and PV across all the grids attaining a minimum costs, whereas Case 0 scales PV capacity regardless of grid properties and irradiance potential. Costs are discussed next.

Table 3.1: Deployment of PV and BESS in the two cases.

Scenario	PV installed capacity (GWp)	PV production (TWh/y)		BESS Power (GW)		BESS Capacity (GWh)		Total cost Billions \$	
		Case 0	Case 1	Case 0	Case 1	Case 0	Case 1	Case 0	Case 1
A	1.71	1.90	2.11	0.00	0.00	0.00	0.00	1.76	1.77
B	3.43	3.81	4.09	0.00	0.00	0.00	0.01	3.53	3.53
C	6.85	7.62	7.87	0.03	0.01	0.14	0.01	7.11	7.07
D	10.28	11.42	11.46	0.46	0.04	1.31	0.05	11.07	10.61
E	13.70	15.23	15.25	1.74	0.51	5.73	0.68	16.18	14.42
F	17.02	18.92	18.99	3.64	3.08	14.74	7.88	22.68	20.51
G	20.11	22.36	22.43	5.87	5.67	26.83	21.26	29.94	28.23
H	22.89	25.44	25.46	8.10	7.94	39.90	36.20	37.17	36.03
I	25.42	28.24	28.25	10.18	10.08	53.41	51.00	44.25	43.50
J	27.57	30.61	30.61	12.07	12.00	65.87	65.04	50.57	50.31

3.4 Cost comparison

Figure 3.2 shows the total cost over the PV yearly production of the two cases using data from Table 3.1. Case 1 achieves a lower unitary cost due to selecting the locations with the largest irradiance

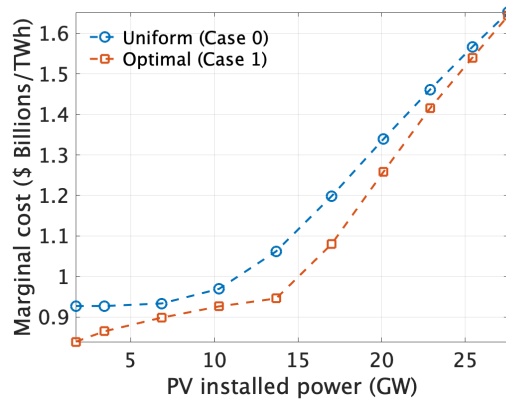


Figure 3.2: Cost per TWh of PV energy production for the two cases.

potential. However, for higher values of installed PV generation capacity, the costs converge to the same value due to land-use limitations in most PV-favourable grids.

Fig. 3.3a shows the BESS energy capacity and power rating requirements as a function of the installed PV generation capacity. Requirements are mild before increasing sharply after 14 GW²). It can be noted that mitigating with BESSs the impact of excess PV generation on distribution grids is an energy-intensive application, with power-rating-to-energy-capacity ratios (i.e., C-rates) around 1/5. As current BESSs technologies can safely operate up to 2-3C, the spare power rating can be conveniently used to provide additional ancillary services, such as primary frequency control and grid synchronization services, that are mostly power-intensive (Namor et al., 2018). Fig. 3.3b shows the corresponding system cost and cost breakdown and shows that the cost of the PV panels is largely dominant.

²This value of hosting capacity is in-line with the country-wide hosting capacity obtained by solving the problem in Section 2.2.

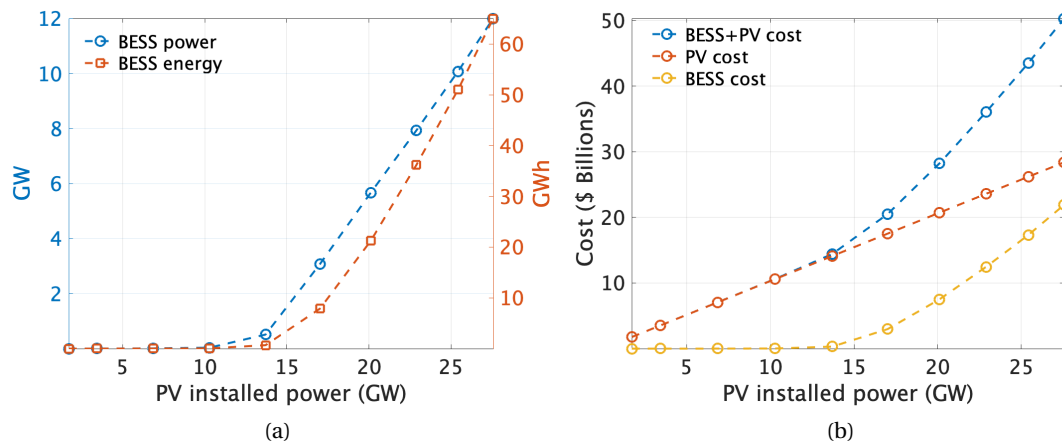


Figure 3.3: (a) BESS cost and size: (a) BESSs power rating and energy capacity and (b) system cost breakdown for Case 1 for different levels of installed PV generation capacity.

Chapter 4

Conclusions

PV generation is and will play a key role in achieving the energy transition target, in Switzerland. As PV plants are connected to distribution grids, it is important to take into account their generation hosting capacity, which is typically limited due to requirements of DSOs to keep voltage levels within statutory limits, respect the cable ampacities and rating of the substation transformer. The main obstacle to analyzing the PV hosting capacity of existing distribution grids is that their topologies and line characteristics are confidential information owned by different DSOs. For this reason, we have first developed a method to estimate likely distribution grids starting from publicly available georeferenced data. Relying on the fact that existing distribution grids interface spatially distributed electrical demand, we use the country-wide map of the electrical demand to infer likely locations of the HV and MV electrical nodes and connect them with a routing procedure from the existing literature.

We then present a computationally tractable method based on a linearized OPF problem to compute the PV hosting capacity of distribution grids, including how to accommodate PV generation beyond prescribed limits with adequately located and sized distributed energy storage systems to relief grid constraints violations.

Finally, we propose and solve a specific planning problem that determines a cost-efficient allocation of PV power across the whole country accounting for the technical limitations of the distribution grids (including adding energy storage, if conducive to lower system costs) and the distributed potential of PV generation, modeled with highly resolved PV capacity factors from PVGIS, which include shading from topographical features along the horizon. The "cost-efficiency" notion for installing PV and energy storage systems relies on two considerations. First, it is more convenient to install PV generation where the PV capacity factor is higher. Second, it may be cheaper to invest in distributed energy storage to extend the PV hosting capacity of highly insulated distribution grids beyond prescribed limits rather than installing PV where its generation potential is low. We also consider land-use allocation to identify the sites where it is possible to install PV generation.

Appendix A

Linear grid model

We model the grid with sensitivity coefficients which express the nodal voltages, lines currents and grid losses as linear function of the nodal active and reactive power injections. The linear grid models for voltage, current and total grid losses are

$$\mathbf{v}_t = v(\mathbf{v}_0, \mathbf{p}_t, \mathbf{q}_t) = \mathbf{A}_t^v \begin{bmatrix} \mathbf{p}_t \\ \mathbf{q}_t \end{bmatrix} + \mathbf{b}_t^v \quad (\text{A.1})$$

$$\mathbf{i}_t = c(\mathbf{i}_0, \mathbf{p}_t, \mathbf{q}_t) = \mathbf{A}_t^i \begin{bmatrix} \mathbf{p}_t \\ \mathbf{q}_t \end{bmatrix} + \mathbf{b}_t^i \quad (\text{A.2})$$

$$\begin{bmatrix} p_t^{\text{gcp}} \\ q_t^{\text{gcp}} \end{bmatrix} = s(\mathbf{p}_t, \mathbf{q}_t, \bar{s}_0) = \mathbf{A}_t^{\text{gcp}} \begin{bmatrix} \mathbf{p}_t \\ \mathbf{q}_t \end{bmatrix} + \mathbf{b}_t^{\text{gcp}} \quad (\text{A.3})$$

where \mathbf{A} and \mathbf{b} are the linear mapping parameters and obtained using the method in (Gupta et al., 2019) which are iteratively updated with newly sized battery and PV injections. The symbols $p_t^{\text{gcp}}, q_t^{\text{gcp}}$ denotes the active and reactive power at the GCP.

Bibliography

- Affi, S., Dang, D.C., Moukrim, A., 2013. A simulated annealing algorithm for the vehicle routing problem with time windows and synchronization constraints, in: International Conference on Learning and Intelligent Optimization, Springer. pp. 259–265.
- Amme, J., Pleßmann, G., Bühler, J., Hülk, L., Kötter, E., Schwaegerl, P., 2018. The ego grid model: An open-source and open-data based synthetic medium-voltage grid model for distribution power supply systems, in: Journal of Physics: Conference Series, IOP Publishing. p. 012007.
- Assouline, D., Mohajeri, N., Scartezzini, J.L., 2017. Quantifying rooftop photovoltaic solar energy potential: A machine learning approach. Solar Energy 141, 278–296.
- Assouline, D., Mohajeri, N., Scartezzini, J.L., 2018. Large-scale rooftop solar photovoltaic technical potential estimation using random forests. Applied energy 217, 189–211.
- Avdakovic, S., Ademovic, A., Nuhanovic, A., 2013. Correlation between air temperature and electricity demand by linear regression and wavelet coherence approach: Uk, slovakia and bosnia and herzegovina case study. Archives of Electrical Engineering 62.
- Bauer, C., Hirschberg, S., 2017. Potentiale kosten und umweltauswirkungen von stromproduktion-sanlagen. PSI-Paul Scherrer Institut, Bundesamt für Energie BFE , 1–10.
- Boulaxis, N.G., Papadopoulos, M.P., 2002. Optimal feeder routing in distribution system planning using dynamic programming technique and gis facilities. IEEE Transactions on Power Delivery 17, 242–247.
- Buffat, R., Grassi, S., Raubal, M., 2018. A scalable method for estimating rooftop solar irradiation potential over large regions. Applied energy 216, 389–401.
- C6.04.02, C.T.F., 2009. Benchmark Systems for Network Integration of renewable and Distributed Energy Resources. Technical Report. Cigre' International Council on large electric systems.
- Chen, Y., Wang, S., Yu, J., Li, W., Shi, X., Yang, W., 2017. Optimal weighted voronoi diagram method of distribution network planning considering city planning coordination factors, in: 2017 4th International Conference on Systems and Informatics (ICSAI), IEEE. pp. 335–340.
- Diaz-Dorado, E., Cidrás, J., Míguez, E., 2002. Application of evolutionary algorithms for the planning of urban distribution networks of medium voltage. IEEE Transactions on Power Systems 17, 879–884.
- ENTSOE, 2019. Entso-e transmission system map. URL: <https://www.entsoe.eu/data/map/>.

- Eymann, L., Rohrer, J., Stucki, M., 2014. Energieverbrauch der schweizer kantone: Endenergieverbrauch und mittelabfluss durch den energie-import .
- Fabietti, L., Gorecki, T.T., Namor, E., Sossan, F., Paolone, M., Jones, C.N., 2018. Enhancing the dispatchability of distribution networks through utility-scale batteries and flexible demand. *Energy and Buildings* 172, 125–138.
- Georgilakis, P.S., Hatziargyriou, N.D., 2015. A review of power distribution planning in the modern power systems era: Models, methods and future research. *Electric Power Systems Research* 121, 89–100.
- Gomez, J., Khodr, H., De Oliveira, P., Ocque, L., Yusta, J., Villasana, R., Urdaneta, A., 2004. Ant colony system algorithm for the planning of primary distribution circuits. *IEEE Transactions on power systems* 19, 996–1004.
- Gonzalez, R.C., Woods, R.E., Eddins, S.L., 2004. *Digital image processing using MATLAB*. Pearson Education India.
- Goswami, S., 1997. Distribution system planning using branch exchange technique. *IEEE Transactions on Power Systems* 12, 718–723.
- Guide, P.Q.A., 2004. Voltage disturbances. Standard EN 50160.
- Gupta, R., Sossan, F., Paolone, M., 2019. Performance Assessment of Linearized OPF-based Distributed Real-time Predictive Control, in: *IEEE PowerTech 2019*, Milan, Italy.
- Kraning, M., Wang, Y., Akuiyibo, E., Boyd, S., 2011. Operation and configuration of a storage portfolio via convex optimization, in: *Proceedings of the 18th IFAC World Congress*, Citeseer. pp. 10487–10492.
- Luthander, R., Widén, J., Nilsson, D., Palm, J., 2015. Photovoltaic self-consumption in buildings: A review. *Applied Energy* 142.
- Nahman, J.M., Peric, D.M., 2008. Optimal planning of radial distribution networks by simulated annealing technique. *IEEE Transactions on Power Systems* 23, 790–795.
- Nahman, J.M., Perić, D.M., 2020. Radial distribution network planning under uncertainty by applying different reliability cost models. *International Journal of Electrical Power & Energy Systems* 117, 105655.
- Najafi, S., Hosseinian, S.H., Abedi, M., Vahidnia, A., Abachezadeh, S., 2009. A framework for optimal planning in large distribution networks. *IEEE Transactions on Power Systems* 24, 1019–1028.
- Namor, E., Sossan, F., Cherkaoui, R., Paolone, M., 2018. Control of battery storage systems for the simultaneous provision of multiple services. *IEEE Transactions on Smart Grid* 10, 2799–2808.
- Nick, M., Cherkaoui, R., Paolone, M., 2017. Optimal planning of distributed energy storage systems in active distribution networks embedding grid reconfiguration. *IEEE Transactions on Power Systems* 33, 1577–1590.
- Peponis, G., Papadopoulos, M., 1997. New dynamic, branch exchange method for optimal distribution system planning. *IEE Proceedings-Generation, Transmission and Distribution* 144, 333–339.

- Sossan, F., 2017. Equivalent electricity storage capacity of domestic thermostatically controlled loads. *Energy* 122, 767–778.
- Sossan, F., Kosek, A.M., Martinenas, S., Marinelli, M., Bindner, H.W., 2013. Scheduling of domestic water heater power demand for maximizing pv self-consumption using model predictive control, in: 2013 4th IEEE PES Innovative Smart Grid Technologies Europe, IEEE.
- Sossan, F., Scolari, E., Gupta, R., Paolone, M., 2019. Solar irradiance estimations for modeling the variability of photovoltaic generation and assessing violations of grid constraints: A comparison between satellite and pyranometers measurements with load flow simulations. *Journal of Renewable and Sustainable Energy* 11, 056103.
- Stai, E., Sossan, F., Namor, E., Boudec, J.Y.L., Paolone, M., 2020. A receding horizon control approach for re-dispatching stochastic heterogeneous resources accounting for grid and battery losses. *Electric Power Systems Research* 185.
- Walch, A., Castello, R., Mohajeri, N., Scartezzini, J.L., 2020. Big data mining for the estimation of hourly rooftop photovoltaic potential and its uncertainty. *Applied Energy* 262, 114404.
- Walch, A., Mohajeri, N., Scartezzini, J.L., 2019. A critical comparison of methods to estimate solar rooftop photovoltaic potential in switzerland, in: *Journal of Physics: Conference Series*, IOP Publishing. p. 012035.
- Wang, S., Lu, Z., Ge, S., Wang, C., 2014. An improved substation locating and sizing method based on the weighted voronoi diagram and the transportation model. *Journal of Applied Mathematics* 2014.
- Wang, Z., Scaglione, A., Thomas, R.J., 2010. Generating statistically correct random topologies for testing smart grid communication and control networks. *IEEE transactions on Smart Grid* 1, 28–39.
- Wiegmans, B., 2016. Gridkit extract of entso-e interactive map. URL: <https://doi.org/10.5281/zenodo.55853>, doi:10.5281/zenodo.55853.
- Wojdyga, K., 2008. An influence of weather conditions on heat demand in district heating systems. *Energy and Buildings* 40, 2009–2014.
- Yan, Y., Wang, F., Zhou, K., Chen, S., Huang, J., Wen, B., 2019. Substation sower supply area division based on voronoi diagram and road grid, in: *IOP Conference Series: Materials Science and Engineering*, IOP Publishing. p. 042101.